$ZnO-Al_2O_3$ and $ZnO-TiO_2$ Core−Shell Nanowire Dye-Sensitized Solar Cells

Matt Law,[†,§] Lori E. Greene,[†,§] Aleksandra Radenovic,[‡] Tevye Kuykendall,[†,§] Jan Liphardt,[‡] and Peidong Yang*[,†,§]

Department of Chemistry, University of California, Berkeley, Berkeley, California 94720, Department of Physics, University of California, Berkeley, Berkeley, California 94720, and Materials Sciences Division, Lawrence Berkeley National Laboratory, Berkeley, California 94720

Received: July 29, 2006; In Final Form: September 5, 2006

We describe the construction and performance of dye-sensitized solar cells (DSCs) based on arrays of ZnO nanowires coated with thin shells of amorphous Al_2O_3 or anatase TiO_2 by atomic layer deposition. We find that alumina shells of all thicknesses act as insulating barriers that improve cell open-circuit voltage (V_{OC}) only at the expense of a larger decrease in short-circuit current density (J_{SC}). However, titania shells 10−25 nm in thickness cause a dramatic increase in V_{OC} and fill factor with little current falloff, resulting in a substantial improvement in overall conversion efficiency, up to 2.25% under 100 mW cm^{-2} AM 1.5 simulated sunlight. The superior performance of the $ZnO-TiO_2$ core−shell nanowire cells is a result of a radial surface field within each nanowire that decreases the rate of recombination in these devices. In a related set of experiments, we have found that TiO_2 blocking layers deposited underneath the nanowire films yield cells with reduced efficiency, in contrast to the beneficial use of blocking layers in some TiO_2 nanoparticle cells. Raising the efficiency of our nanowire DSCs above 2.5% depends on achieving higher dye loadings through an increase in nanowire array surface area.

Introduction

Dye-sensitized solar cells (DSCs) are typically constructed from thick films of TiO_2, SnO_2, or ZnO nanoparticles that are sintered into a mesoporous network with a large internal surface area for the adsorption of light-harvesting dye molecules. Under illumination, dye excited states undergo rapid charge separation, with electrons injected into the nanocrystalline film and holes leaving the opposite side of the device by means of redox species in a liquid or solid-state electrolyte. Electron transport through the nanoparticle network occurs by trap-mediated diffusion, a slow mechanism (with electron escape times of 1−10 ms for ∼10-μm-thick TiO_2 films)[1] that is nonetheless efficient for TiO_2 cells that use the traditional I^-/I_3^- redox couple in a liquid electrolyte. State-of-the-art liquid-electrolyte TiO_2 DSCs show near-unity external quantum efficiency at wavelengths near the absorption maximum of the dye.[2] Such efficient charge collection is possible despite slow electron transport because of the order-of-magnitude slower recombination of photoinjected electrons with I_3^- in the electrolyte.[3,4] This delicate balance between transport and recombination is easily destroyed by attempts to improve cell stability or push cell efficiency above its longstanding record[2,4] of 10−11% by, for example, (i) replacing the volatile liquid electrolyte and I^-/I_3^- couple with nonvolatile[5,6] or solid-state alternatives,[7−9] (ii) thickening the nanocrystalline film to improve its light absorption and quantum yield at red wavelengths,[10] or (iii) adopting a different nanocrystalline material in the hope of speeding up electron transport and slowing recombination.

In principle, a substantial increase in DSC efficiency is attainable with one of three fixes. The fix with the greatest potential to boost performance is to employ a new sensitizer with a higher molar extinction coefficient and broader spectral response than existing dyes. The development of new panchromatic dyes or dye cocktails that break the 10% efficiency limit is an unmet challenge and important focus of current research.[9−14] A second fix, with a somewhat smaller efficiency payoff, is to improve cell open-circuit voltage (V_{OC}), which is determined by the energy difference between the quasi-Fermi level of electrons within the TiO_2 film and the Fermi level of the redox couple. It is thermodynamically and kinetically feasible to squeeze an additional 300−400 mV from the TiO_2 DSC by lowering its dark current and, more importantly, utilizing a redox couple more closely matched to the energy of the oxidized dye. All else being equal, a 300 mV increase in V_{OC} would mean a 35% improvement in device efficiency (to ∼14%).

The third way to boost DSC efficiency is to maximize red light conversion by increasing the diffusion length of electrons within the nanocrystalline oxide, L_n, relative to the thickness of the oxide film, d, such that $L_n/d \gg 1$ and $d > \alpha^{-1}$, where α is the wavelength-dependent absorption coefficient of the sensitized film. Cell photocurrent is maximized if $L_n \gg d > \alpha^{-1}$ for all absorbed wavelengths because light harvesting and carrier collection are then very efficient. Presently the best TiO_2 cells feature $L_n/d \leq 2$ with $d = 10-15$ μm and $d < \alpha^{-1}$ for wavelengths greater than 650 nm.[15−18] This is sufficient to achieve high external quantum yields across most of the visible spectrum, but L_n/d is too small to permit thickening the oxide film to maximize red light absorption. The low L_n/d ratio of nanocrystalline TiO_2 has motivated recent efforts to reduce d (while maintaining $d > \alpha^{-1}$) by using sensitizers with larger absorption coefficients[10] or nanocrystalline films with very high specific surface areas.[19] Attempts to increase L_n itself, which depends on the electron diffusivity D_n and the electron lifetime τ_n according to $L_n = (D_n\tau_n)^{1/2}$, have focused on slowing interfacial recombination (i.e., increasing τ_n) by adding surface

* To whom correspondence should be addressed. E-mail: p_yang@berkeley.edu.
[†] Department of Chemistry.
[§] Lawrence Berkeley Laboratory.
[‡] Department of Physics.

10.1021/jp0648644 CCC: $33.50
Published on Web 10/12/2006

coatings to the nanocrystalline film or speeding up electron transport (i.e., increasing D_n) by replacing TiO_2 with a different oxide in which electrons move faster. The surface treatment strategy shows promise and is the main subject of this paper. The latter approach fails, apparently because electron diffusion within the nanocrystalline film is the rate-limiting step in the recombination process, making $D_n \propto \tau_n^{-1}$ and negating any positive impact of faster electron motion.[1,20] Faster transport can be expected to improve DSC efficiency only when it does not trigger proportionally faster recombination.

We recently introduced a new DSC architecture based on an array of single-crystalline ZnO nanowires that should show a weaker link between diffusion and recombination and enable the faster transport that occurs in nanowires to yield a larger L_n and improved quantum yield for red light.[21] Better electron transport in these nanowire films is a product of their excellent crystallinity and a radial electric field within each nanowire that assists carrier collection by repelling photoinjected electrons from the surrounding electrolyte. In this picture, upward band bending at the surface of each nanowire reduces the surface recombination velocity of the majority-carrier electrons regardless of the speed at which the electrons move. Recombination may remain diffusion limited, but the rate at which electrons sample the oxide surface is determined by the magnitude of the surface field rather than the diffusion constant for electrons in the wire cores. Diffusion lengths substantially larger than those of nanocrystalline films are therefore possible. Attaining a superior short-circuit current density (J_{SC}) with a nanowire cell of large L_n depends on fabricating single-crystalline nanowire arrays with surface areas at least as large as typical nanocrystalline films, which is a significant challenge.

Several DSCs incorporating one-dimensional nanostructures have been reported by other groups. Of these, it is unclear whether cells based on sintered TiO_2 nanorod and nanotube powders[22−24] or nanocrystalline TiO_2 nanotube arrays[25] offer any advantage in terms of their transport physics vis-à-vis the standard nanocrystalline films, since they all consist of polycrystalline percolation networks. DSCs based on branched wire-like ZnO[26] may share the transport features of our nanowire films, but no systematic or comparative work investigating electron collection by these structures has been published.

Here we show that carrier recombination in ZnO nanowire dye-sensitized cells can be suppressed and the conversion efficiency enhanced by coating the nanowires in a conformal metal oxide shell made by atomic layer deposition (ALD). Over the past five years, many studies have described the effects of overcoating nanocrystalline TiO_2 or SnO_2 films in thin layers (1−30 Å) of insulating or semiconducting oxides, including Nb_2O_5, Al_2O_3, MgO, $SrTiO_3$, SiO_2, Y_2O_3, ZrO_2, ZnO, SnO_2, and TiO_2.[27−32] In principle, an oxide shell can suppress recombination by (i) introducing an energy barrier that increases the physical separation between photoinjected electrons and the oxidized redox species in the electrolyte, (ii) forming a tunneling barrier that corrals electrons within the conducting cores of the nanoparticle film, or (iii) passivating recombination centers on the oxide surface. A lower rate of recombination appears as a smaller dark current (J_{dark}), which can increase the open-circuit voltage (and fill factor) of a DSC according to the general expression $V_{OC} = nV_{th} \ln((J_{SC}/J_{dark}) + 1)$, where n is the diode ideality factor and V_{th} is the thermal voltage. Whether J_{SC} and cell efficiency also improve depends on the extent to which the electron injection and collection yields are hurt by the oxide shell. In addition to suppressing recombination, a shell can raise cell V_{OC} directly if it has a more negative conduction band edge than the core oxide or if it creates a dipole at the core−shell interface that shifts the band edge of the core upward in energy.[30] Applying the core−shell concept to a nanowire photoelectrode provides a means to increase τ_n and L_n by augmenting the radial surface field that reflects electrons from the nanowire−electrolyte interface.

Experimental Methods

Nanowire Array Fabrication. The ZnO nanowires were grown in aqueous solution, using a two-step synthesis described elsewhere.[21] Conductive glass substrates (F:SnO_2, 8 Ω/□, Hartford Glass Co.) were ultrasonically cleaned first in ethanol/acetone and then in 1 M HCl, rinsed in ethanol, and dried under a stream of nitrogen, then coated in several monolayers of ZnO nanoparticles, 3−4 nm in diameter, by dip-coating in a concentrated ethanol solution and rinsing with clean ethanol. Nanowires were grown from these seeds by immersing substrates (up to a dozen at a time) in an aqueous solution containing 25 mM zinc nitrate hydrate, 25 mM hexamethylenetetramine, and 5−7 mM polyethyleneimine (branched, low molecular weight, Aldrich) at 92 °C for 24 h. A homemade continuous-flow reactor was used to achieve a constant nanowire growth rate during the reaction period (solution turnover time ~2.5 h). After growth, the substrates were rinsed with water and baked at 400 °C in air for 30 min to remove any residual organics. This procedure resulted in arrays of nanowires with lengths and diameters of 15 ± 2 μm and 150 ± 30 nm, respectively.

Shells of Al_2O_3 or TiO_2 were grown on the nanowire films in a homemade traveling-wave atomic layer deposition (ALD) system with a process pressure of 100−500 mTorr. Al_2O_3 was deposited from trimethylaluminum (97%, Aldrich) and distilled water at 210 °C, using 1 s precursor pulses and a purge time of 12 s. TiO_2 was deposited from $TiCl_4$ (99.999%, Aldrich) and water at 300 °C, using a similar sequence. The average growth rate was 1.1 Å per cycle and 0.49 Å per cycle for Al_2O_3 and TiO_2, respectively. To expose an area for electrical contact, part of each nanowire film was removed by rubbing the substrate surface clean with a swab soaked in 1 M HCl. The arrays were then rinsed thoroughly in water and blown dry in nitrogen.

Cell Fabrication and Testing. Each sample was heated to 400 °C in air for 30 min and immersed while still warm in a 0.5 mM solution of N719 dye (*cis*-bis(isothiocyanato)bis(2,2′-bipyridyl-4,4′-dicarboxylato)ruthenium(II) bistetrabutylammonium) in acetonitrile/*tert*-butyl alcohol (1:1 v/v) for 1, 8, or 12 h, depending on the experiment (see below). Sensitized films were rinsed with ethanol, blown dry, and sandwiched together and bonded to thermally platinized counter electrodes separated by hot melt spacers (40 μm thick, Bynel, Dupont). The internal space of each cell was filled with a liquid electrolyte (0.5 M LiI, 50 mM I_2, 0.5 M 4-tertbutylpyridine in 3-methoxypropionitrile (Fluka)) by capillary action. Cells were immediately tested under AM 1.5 G simulated sunlight (300 W Model 91160, Oriel). Cells were illuminated through a black aperture 0.3 cm^2 in area.

Materials Characterization. All transmission electron microscopy (TEM) analysis was performed on a Philips CM200/FEG TEM operating at 200 kV. X-ray diffraction data were obtained on a Bruker D-8 GADDS diffractometer (Co Kα). Photoluminescence measurements were acquired with a continuous wave HeCd laser operating at 325 nm, fiber-coupled to a spectrometer and LN_2-cooled CCD detector. X-ray photoelectron spectra were recorded with a 15 kV, 40 W PHI 5400 ESCA/XPS, using an aluminum source.

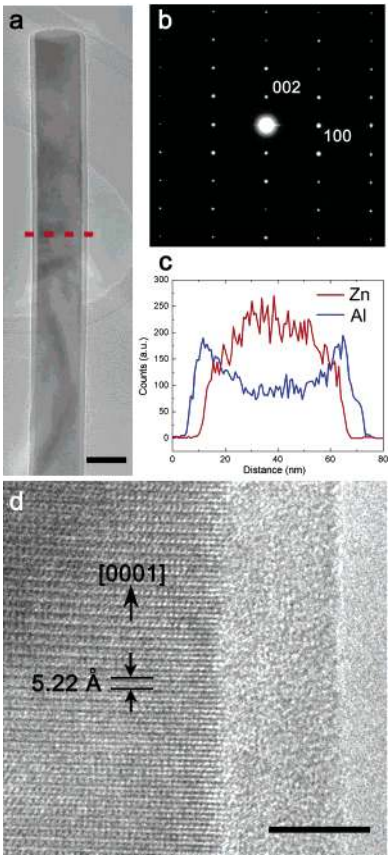

Figure 1. TEM characterization of ZnO−Al_2O_3 core−shell nanowires. (a) Low-magnification image of a wire that has been cleaved in two. Scale bar, 50 nm. (b) Electron diffraction pattern of the same wire. Only ZnO spots are present. (c) EDS elemental profile along the dashed line in part a. (d) High-resolution image of the ZnO−Al_2O_3 interface. Scale bar, 5 nm. Note that uncoated ZnO wires lack an amorphous shell.

The dye loading of each tested cell was determined by desorbing the dye from a second, identically prepared nanowire film in 0.01 M aqueous NaOH and measuring its absorption spectrum. Absorbance values were converted into a roughness factor (RF) for each cell, defined as the dye-coated surface area of the nanowire film divided by the projected area of the film.

Results and Discussion

ZnO−Al_2O_3 Core−Shell Nanowire DSCs. Amorphous alumina shells were grown on ZnO nanowire arrays by ALD, using trimethylaluminum and water at 210 °C. ALD is a stepwise chemical vapor deposition process that yields dense, smooth, and conformal Al_2O_3 coatings with monolayer control over the film thickness. Recently Al_2O_3 ALD was used to make various core−shell nanowires[33] and, by etching away the nanowire cores, Al_2O_3 nanotubes.[34] We used transmission electron microscopy (TEM) to characterize our ZnO−Al_2O_3 core−shell wires, choosing for ease of analysis a sample with thick shells (5.5 nm, representing 50 ALD cycles). Low-magnification TEM imaging and electron diffraction of single core−shells (Figure 1a,b) show that the alumina coating is continuous, smooth, and amorphous. Energy dispersive spectroscopy (EDS) elemental line profiles acquired across the wires (Figure 1c) are consistent with a hexagonal prismatic core−shell structure of ZnO and Al_2O_3. Finally, lattice-resolved images (Figure 1d) indicate that the core−shell interface is atomically abrupt and that the ZnO wires grow, as expected, along the [0001] wurtzite direction. Solar cells built from these

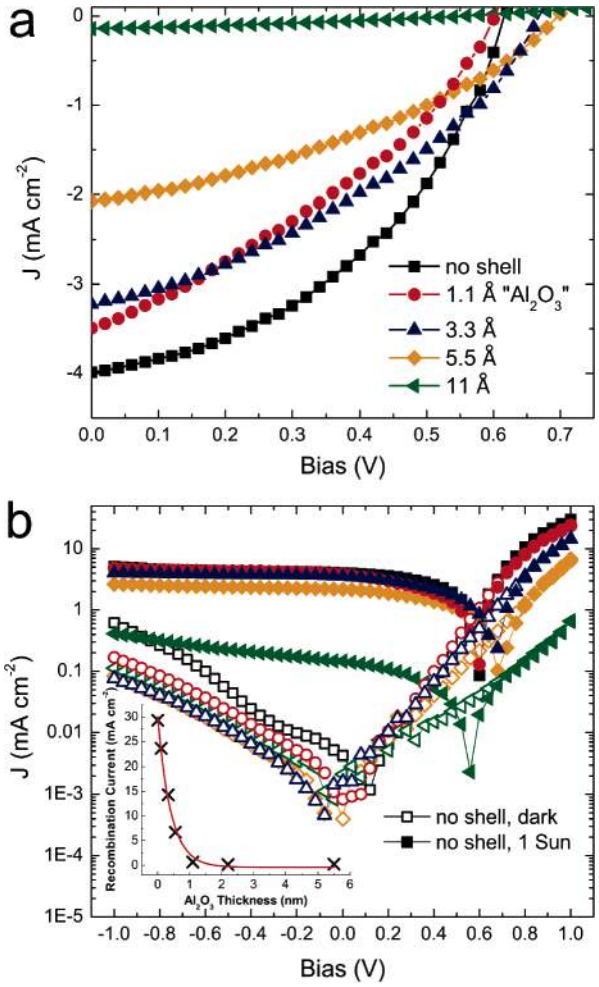

Figure 2. Performance of ZnO−Al_2O_3 core−shell nanowire cells with different shell thicknesses. (a) Power plots for cells with 0, 1, 3, 5, and 10 monolayers of Al_2O_3 under 100 mW cm^{-2} AM 1.5 simulated sunlight. (b) Full-scale semilogarithmic plots in the dark (open symbols) and under illumination (closed symbols). The inset is the exponential dependence of the recombination current on Al_2O_3 thickness (at +1 V). The fitted decay constant is 4.1 ± 0.4 Å.

thick-shelled arrays showed a very high series resistance but were not completely insulating (J_{SC} = 5 μA cm^{-2}, V_{OC} < 0.3 V, and efficiency < 0.001% under one sun conditions).

Solar cells were constructed from ZnO−Al_2O_3 core−shell wire arrays with shell thicknesses up to 22 Å. Figure 2a shows $J-V$ curves of a batch of cells made from nanowire arrays synthesized in the same growth bath. The dye loading of these cells was equalized to within 10% by sensitizing the uncoated array for 1 h and the Al_2O_3-coated arrays for 8 h, yielding a common roughness factor of ∼130 (as measured by dye desorption). The major trends in the data are a small increase in V_{OC} and a larger decrease in J_{SC} with increasing shell thickness. V_{OC} plateaus and then falls for thick shells. The fill factor shows little change in this range of shell thickness. Overall, the Al_2O_3 shells decrease the power conversion efficiency of our nanowire DSCs. Figure 2b compares the full-scale photocurrent and dark current of each cell. As expected, alumina shells of increasing thickness progressively suppress current at all biases, especially the dark cathodic recombination current (here, the current at positive bias) and the photocurrent. This is consistent with alumina acting as a tunnel barrier that improves V_{OC} by impeding recombination when it is very thin but blocks electron injection as it becomes thicker. The exponential decrease of the recombination current with Al_2O_3

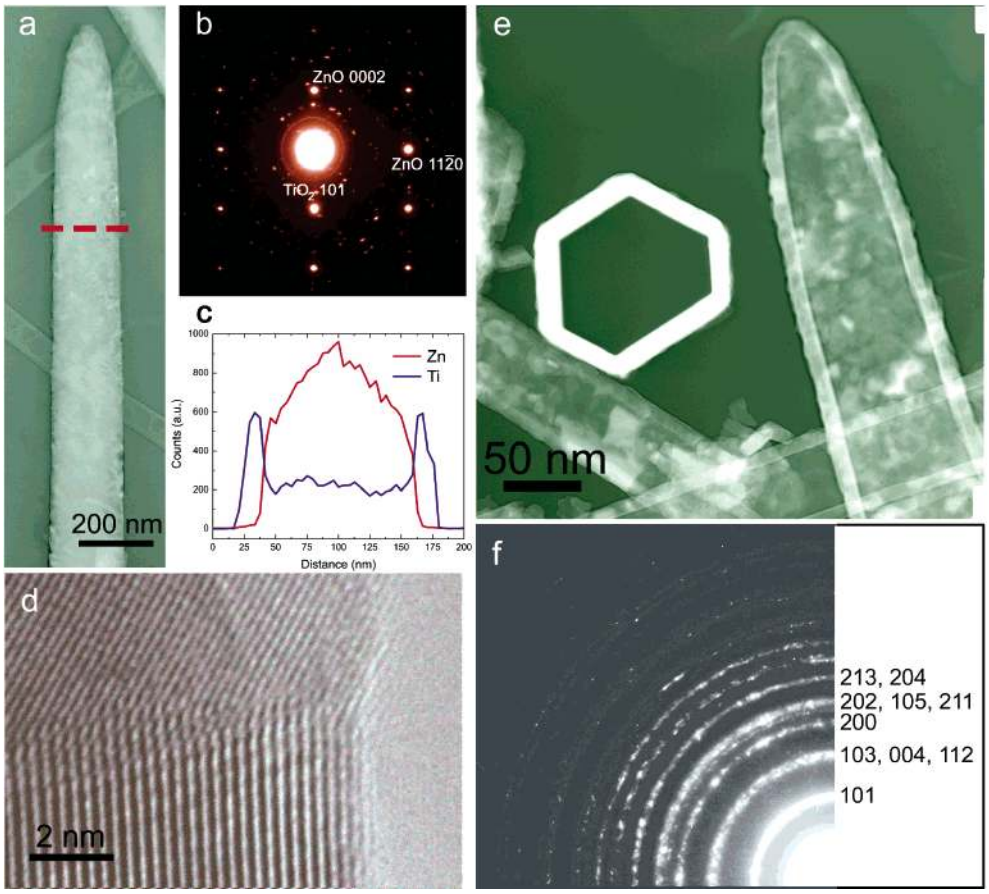

Figure 3. Characterization of ZnO−TiO_2 core−shell nanowires and TiO_2 nanotubes with a shell thickness of 13.5 ± 1 nm. (a) Negative TEM image of a core−shell wire. (b) Selected area electron diffraction pattern of a different core−shell wire, showing a polycrystalline anatase spot pattern superimposed on a single-crystalline ZnO spot pattern. The discontinuous anatase (101) ring is labeled. The continuous ring near center is an artifact from the aperture. (c) EDS elemental profile along the dashed line in part a. (d) High-resolution image of the outer surface of a core−shell wire. (e) Negative TEM image of anatase nanotubes made by removing the ZnO wire cores in 1 M aqueous HCl. The tubes have hexagonal cross sections. (f) Electron diffraction of an ensemble of tubes. The 10 innermost rings are labeled (all rings are anatase).

thickness supports this interpretation (see the inset in Figure 2b). The V_{OC} of these core−shell cells remains higher than the V_{OC} of the uncoated cells as long as the steady-state photoinjected charge density is greater. Thick shells that reduce the rate of electron injection more than the rate of recombination lower the steady-state charge density in the nanowires and hurt V_{OC}.

Our results are consistent with several reports of increased V_{OC} and decreased J_{SC} for Al_2O_3-coated nanocrystalline SnO_2 and TiO_2 electrodes,[35−37] but at odds with other studies that find enhanced V_{OC}, J_{SC}, and fill factor for TiO_2 films with sol−gel-type Al_2O_3 overlayers.[29,38] Authors of one of the latter papers established that alumina shells retard the recombination dynamics of nanocrystalline TiO_2 by passivating surface recombination centers and slowing the rate of interfacial charge transfer.[39] However, we note that Al_2O_3 coatings have been shown to improve the efficiency of only relatively inefficient devices (<5%) and that no core−shell cell has yet outperformed the best TiO_2 cells made by Grätzel et al. In any case, these unpromising results discouraged further study of the ZnO−Al_2O_3 core−shell nanowire cells.

ZnO−TiO_2 Core−Shell Nanowire DSCs. The same ALD apparatus was used to fabricate ZnO−TiO_2 core−shell nanowire arrays. Here, alternating pulses of titanium tetrachloride and water at 300 °C produced continuous and conformal coatings of TiO_2 on the ZnO surface (Figure 3). To characterize the ALD-made titania, planar thin films were deposited on silicon and glass substrates and probed by ellipsometry, scanning electron microscopy (SEM), X-ray diffraction (XRD), UV−vis and photoluminescence (PL) spectroscopy, X-ray photoelectron spectroscopy (XPS), and electrical measurements (Figure 4). We measured an average growth rate of 0.49 Å per ALD cycle (<0.5 monolayers per cycle), which is consistent with previously reported values.[40,41] The same growth rate was measured by TEM for TiO_2 shells grown on ZnO nanowires. TiO_2 films thinner than about 5 nm were completely amorphous and very smooth (Supporting Information, Figure 1). Thicker films converted to polycrystalline anatase throughout their thickness and were rougher, in agreement with previous observations.[42,43] XPS surface analysis revealed trace chlorine present in some of the as-grown films. However, neither chlorine nor other impurities (except adventitious carbon) were found by XPS in films baked in air at 400 °C. These TiO_2 films proved too resistive (1−10 GΩ) for accurate Hall measurements with our equipment. Four-point measurements on 50-nm-thick films grown on glass and baked in air at 400 °C for 30 min gave a dark, room temperature resistivity of $\sim 10^4$ Ω·cm (with ohmic Al or Cu contacts). A two-point through-plane resistivity of $<10^3$ Ω·cm was estimated by using films grown on ultraflat indium tin oxide substrates. This type of anisotropic conductivity is typical of thin films in which in-plane conduction requires carriers to cross many grain boundaries while through-plane conduction involves transport across a single crystallite, or several at most. It implies that photoinjected electrons in the ZnO−TiO_2 core−shell nanowire cells will tend to travel across the thin TiO_2 shells and into the more conductive ZnO cores

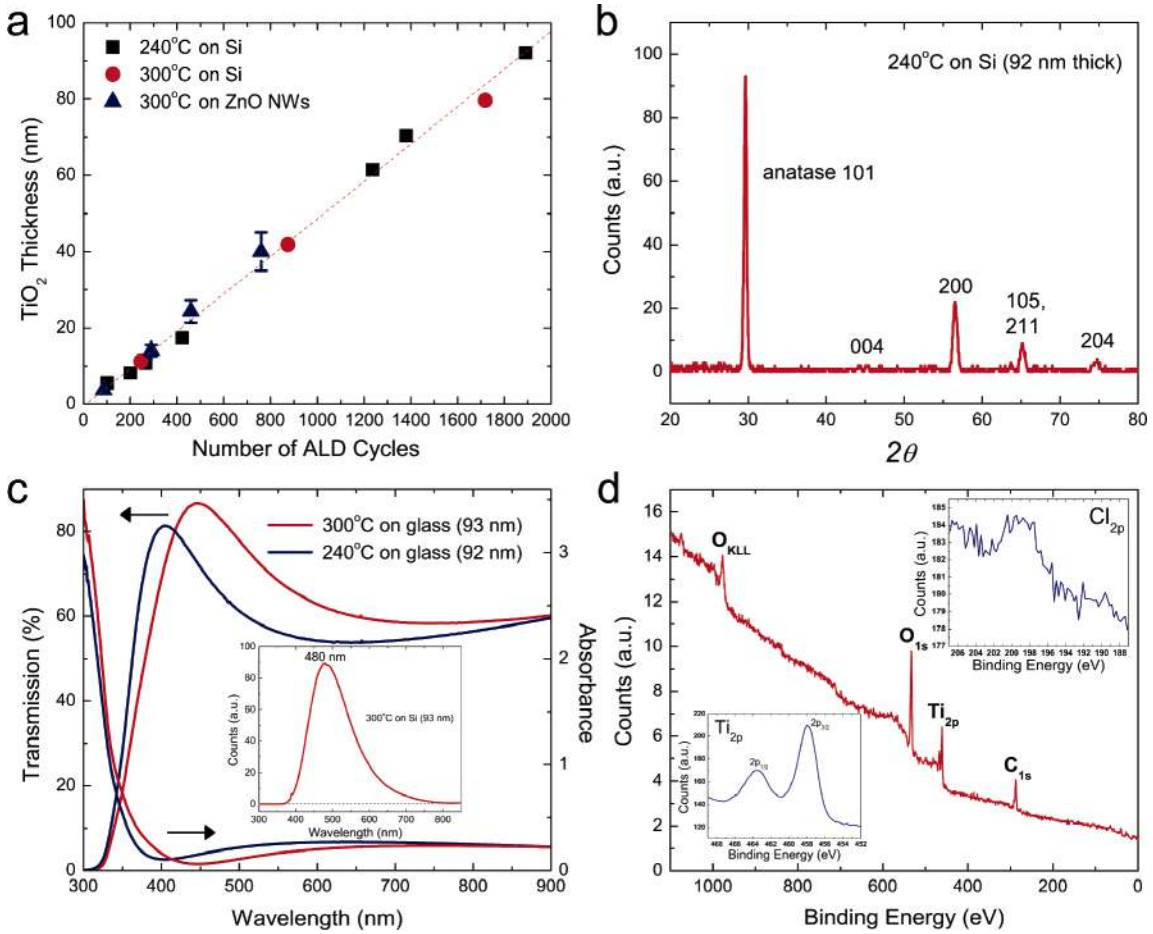

Figure 4. Characterization of ALD TiO_2 thin films. (a) Dependence of film thickness on the number of ALD cycles for films deposited at 240 and 300 °C on silicon substrates and 300 °C on ZnO nanowires. The linear fit is 0.49 Å per cycle. The thickness of samples on silicon was measured by ellipsometry, while TEM was used for shells grown on ZnO nanowires after dissolving the ZnO in 1 M aqueous HCl. (b) X-ray diffraction pattern of a TiO_2 film deposited on silicon at 240 °C. All films thicker than ~5 nm index to polycrystalline anatase, independent of growth substrate (Si, FTO, glass). (c) Extinction and transmission spectra of anatase films grown on glass at 240 and 300 °C. The inset is a photoluminescence spectrum of a film grown on silicon at 300 °C. The small peak at 388 nm is an instrument artifact. (d) XPS spectrum (Al Kα) of a film grown on silicon at 300 °C. The insets show details of the Ti 2p and Cl 2p regions. Chlorine was detected in a minority of samples; otherwise only titanium, oxygen, and adventitious carbon were found.

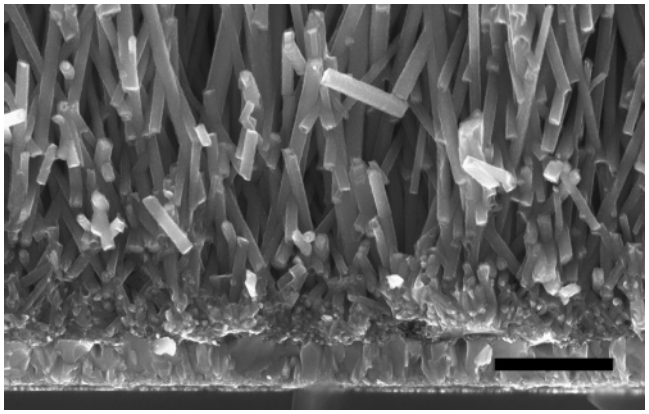

Figure 5. Cross-sectional SEM image of a core−shell nanowire array on FTO. Dozens of ZnO cores are visible in this damaged part of the array. Scale bar, 1 μm.

(which have a resistivity of ~1 Ω·cm);[21] in other words, the most conductive pathway in these cells is approximately the pathway of least TiO_2. A cross-sectional image of a typical core−shell array on an FTO substrate is shown in Figure 5.

We compare ZnO−TiO_2 core−shell nanowire cells prepared with saturated dye loadings for maximum device efficiency. Figure 6 presents $J-V$ data from a batch of core−shell arrays coated in different thicknesses of TiO_2 and sensitized in dye for 12 h. Two control cells are included in the plots: an uncoated ZnO cell sensitized for 1 h and an uncoated ZnO cell sensitized for 12 h. The optimal sensitization time for our ZnO nanowires was 1 h, which was sufficient to achieve a high dye loading without building up Zn−dye multilayers that form from the slow etching of ZnO by the acidic N719 dye.[44] We hereafter refer to uncoated ZnO nanowire cells sensitized for 1 h as *standard* cells. The longer sensitization time for the TiO_2-coated cells reflects the slower rate of dye adsorption on the more acidic TiO_2 surface. Twelve hours was adequate to saturate the dye loading of the core−shell arrays.

The addition of TiO_2 shells to ZnO wire cells resulted in considerable improvement in both V_{OC} and fill factor (Figure 6a). For shells thicker than 10 nm, V_{OC} increased by about 250 mV to 0.78−0.82 and the fill factor jumped to 0.58−0.6, a 60% improvement. The trend in J_{SC} was more complex. The current first fell by a factor of 2−3 with the addition of ultrathin shells (0.5 nm − 5 nm) and then slowly recovered with increasing shell thickness to near the value of the standard cell. Overall, cell efficiency more than doubled in response to TiO_2 shells 10−35 nm thick, jumping from 0.85% to 1.7−2.1%. The full-scale semilogarithmic plots in Figure 6b show that the dark current of the cells decreased with increasing shell thickness, which suggests that the improvement in V_{OC} and fill factor

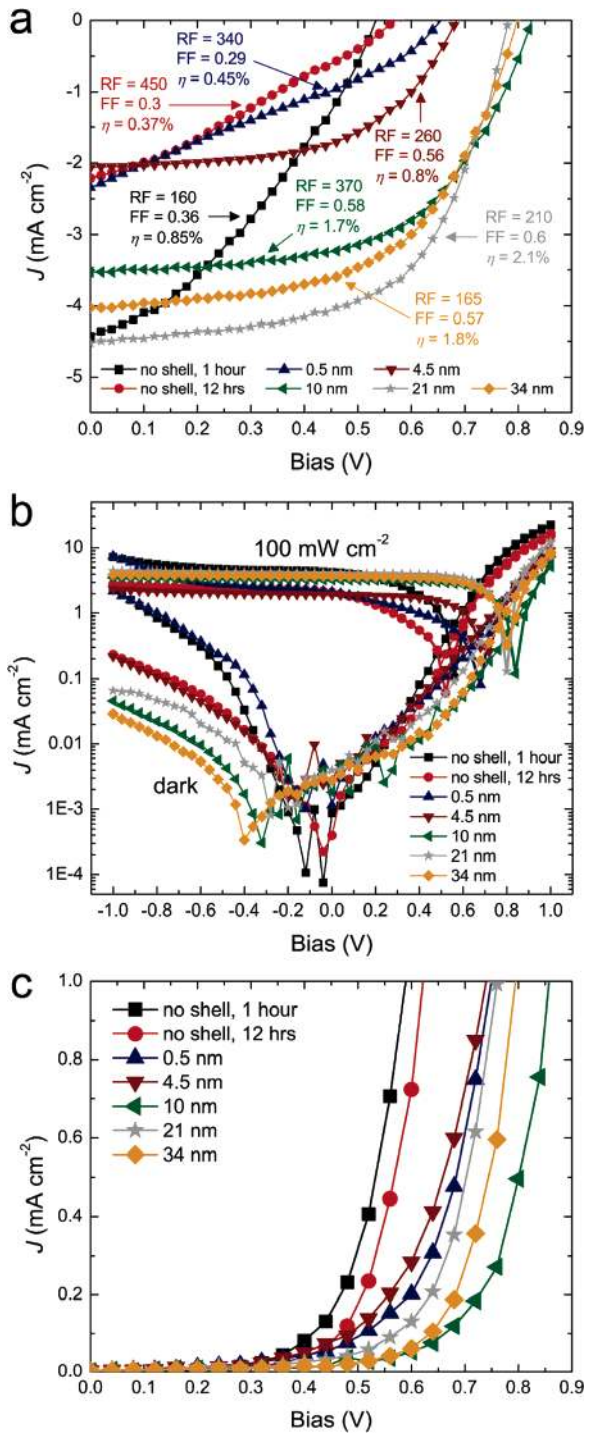

Figure 6. $J-V$ data for a batch of core−shell nanowire cells of different shell thickness. Each cell was sensitized in dye solution for 12 h except for one uncoated ZnO nanowire control cell, which was sensitized for 1 h. (a) Power plots under 100 mW cm^{-2} simulated sunlight. The roughness factor (RF), fill factor (FF), and efficiency (η) are specified for each device. (b) Full-scale semilogarithmic plots in the dark and under illumination. (c) Dark recombination current.

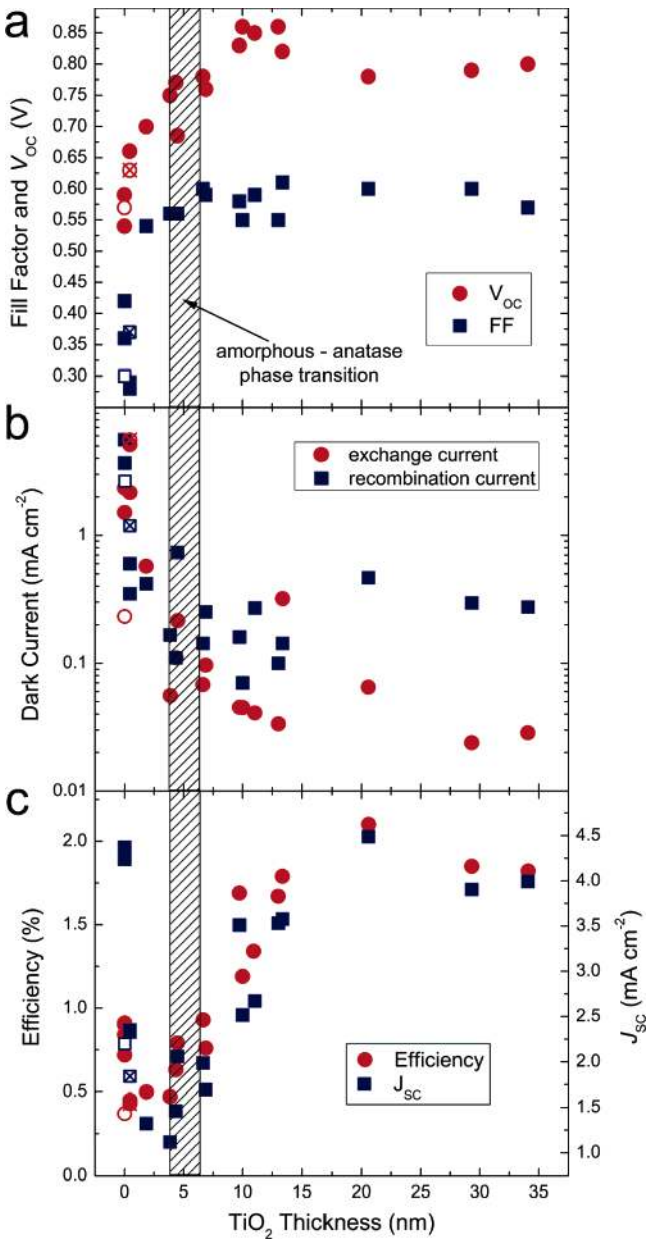

Figure 7. Performance trends for ZnO−TiO_2 core−shell nanowire cells of different shell thickness at a light intensity of 100 mW cm^{-2}. (a) V_{OC} and fill factor. (b) Dark anodic exchange current and cathodic recombination current on a logarithmic scale. (c) J_{SC} and cell efficiency. Filled symbols: Uncoated ZnO nanowire cells sensitized in dye for 1 h (standard cells) and core−shell cells sensitized for 12 h. Open symbols: An uncoated ZnO nanowire cell sensitized for 12 h. Crossed symbols: A core−shell cell sensitized for 1 h. The hatched region indicates the onset of the phase transition from amorphous to anatase TiO_2.

results from a suppression of recombination by the TiO_2 layers. A progressive suppression of the dark recombination current (here, the current at positive bias, where electrons flow from the nanowires into the electrolyte) is apparent in Figure 6c.

We developed a data set based on 20 devices to better quantify the performance trends of the core−shell nanowire cells. Figure 7 displays the dependence of cell fill factor, V_{OC}, dark current, J_{SC}, and efficiency on the thickness of the TiO_2 shell. The fill factor first falls for the thinnest shells (0.5 nm) and then immediately jumps to 0.55−0.6. This increase is driven in part by a 3-fold to 8-fold improvement in the shunt resistance, $R_{sh} = (dV/dI)_{V=0}$ (see Figure 6a). V_{OC} increases even for the thinnest shells, peaks at ~0.85 V at a TiO_2 thickness of 10−15 nm, and seems to fall slightly for the thickest shells. Meanwhile, the dark anodic exchange current (the current at negative bias) and cathodic recombination current decrease by a factor of 100 and 50, respectively, before the latter increases slightly at thick TiO_2 to a value ~20 times smaller than that of the standard cells. A plot of the dark currents against V_{OC} (Figure 8) reveals a strong inverse logarithmic relationship, $V_{OC} \propto \ln(1/J_{dark})$, as

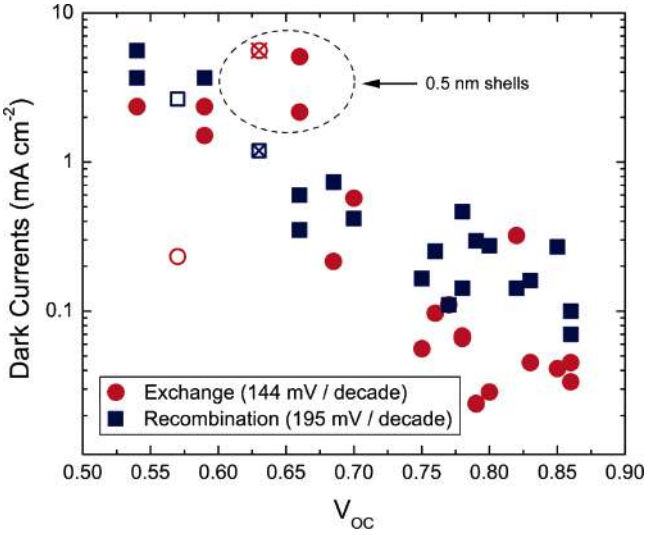

Figure 8. Dependence of V_{OC} on the dark currents. Linear fits to the data give slopes of 144 mV/decade for the exchange current (measured at −1 V) and 195 mV/decade for the recombination current (measured at 0.7 V). Filled, open, and crossed symbols as in Figure 7.

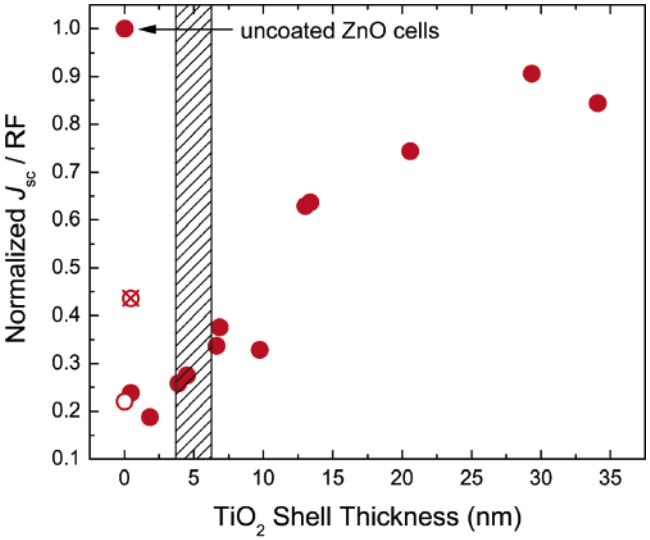

Figure 9. The ratio of short-circuit current to dye loading as a function of TiO_2 thickness. RF = roughness factor, the unitless measure of dye loading. Filled, open, and crossed symbols as in Figure 7. The hatched region indicates the phase transition from amorphous to anatase TiO_2.

expected for photovoltaic and photoelectrochemical cells. Linear fits to the data in Figure 8 give slopes that correspond to 144 mV/decade for the exchange current and 195 mV/decade for the recombination current. The latter value translates to a diode ideality factor $n = 3.25$, which agrees well with $n = 3.2$ as determined from fits of the illuminated current under forward bias. Overall, it is clear from these data that the TiO_2 shells improve V_{OC} and fill factor by lowering the rate of electron−hole recombination across the oxide−electrolyte interface. A determination of precisely how the TiO_2 shells suppress recombination can be made only in concert with understanding the trend in J_{SC}, which we turn to next.

The dependence of J_{SC} on shell thickness is presented in Figure 7c. The current falls dramatically upon addition of the thinnest TiO_2 shells, then bottoms out, steadily recovers, peaks at 15−25 nm, and finally falls off somewhat for the thickest shells. Cell efficiency tracks this trend in J_{SC} quite closely. In DSCs, J_{SC} is a product of the efficiencies of light harvesting, electron injection, and charge collection. The light harvesting efficiency depends directly on the dye loading, which is not constant in this data set but varies systematically with TiO_2 thickness. The general trend in the dye loading of these cells is a 2-fold spike for the thinnest shells followed by a gradual decrease in dye loading to about the same value as the standard cells, which themselves have the least amount of dye (see Figure 6a, in which dye loading is quantified by the roughness factor, RF). At least four factors combine to establish this trend. The initial spike in dye loading can be explained by the longer sensitization time for the core−shell cells plus incomplete coverage of ZnO by the thinnest TiO_2 shells (0.5 nm represents approximately two titania monolayers, which undoubtedly leaves some ZnO exposed to the acidic dye solution). The gradual decrease in dye loading with increasing TiO_2 thickness results in large part from the amorphous-to-anatase phase transition that begins at a shell thickness of 4−6 nm, since the amorphous surface has a greater specific dye loading.[45] In addition, the thickest shells lower the surface area available for dye adsorption by infilling some of the pore space in the bottom third of the nanowire films. The fact that the core−shell cells have more dye and thus a higher light harvesting efficiency than the standard cells means that the valley-to-peak trend in J_{SC} seen in Figure 7c is caused by changes in electron injection and collection rather than light absorption.

To account for differences in dye loading, we plot the ratio of J_{SC} to dye loading as a function of shell thickness in Figure 9. This ratio is a measure of the current collected per unit dye. The data are normalized to the performance of the standard cells, which show a J_{SC} of 4.0−4.5 mA cm^{-2} at a roughness factor of 140−160. It is clear from Figure 9 and the above discussion that dye molecules in core−shell cells are less productive than dye molecules in standard nanowire cells. For example, cells with 4-nm-thick shells contain 60% more dye but produce 60% *less* current than standard cells. The relative productivity of adsorbed dye improves from about 50% for cells with thin shells to around 90% for cells with the thickest shells. This trend suggests that the electron injection yield and/or transport efficiency must be improving with increasing shell thickness.

We propose that the trend in J_{SC} depicted in Figures 7c and 9 is primarily a result of gradual crystallization of the TiO_2 shells, which begins at a threshold thickness of ∼5 nm and progresses for perhaps an additional 15−20 nm of shell growth. As we discuss below, both electron injection and collection should be facilitated by the better crystallinity of thicker TiO_2 shells. To determine the role of the amorphous-to-anatase transition, a set of core−shell cells with completely amorphous TiO_2 shells was fabricated and tested. Amorphous shells were grown by ALD at 120 °C. Procedures identical with those described above were used to prepare these cells except that the core−shell films were heated to 250 °C rather than 400 °C immediately before dye sensitization. Electron- and X-ray diffraction showed that shells made in this way are amorphous regardless of thickness. The performance data and dependence of J_{SC} on shell thickness for the cells with amorphous shells are shown in Figure 10. Thicker shells result in poorer overall efficiency because of a falling J_{SC} and fill factor and only a marginal improvement in V_{OC}. Of particular importance to this discussion is the trend in J_{SC} in Figure 10b. In contrast to the cells with anatase shells, the cells with amorphous shells show very little recovery of J_{SC} with increasing shell thickness. J_{SC} falls and does not recover because (i) electron injection into an amorphous titania surface is inefficient compared with injection into a crystalline anatase surface[46−48] and (ii) the higher density

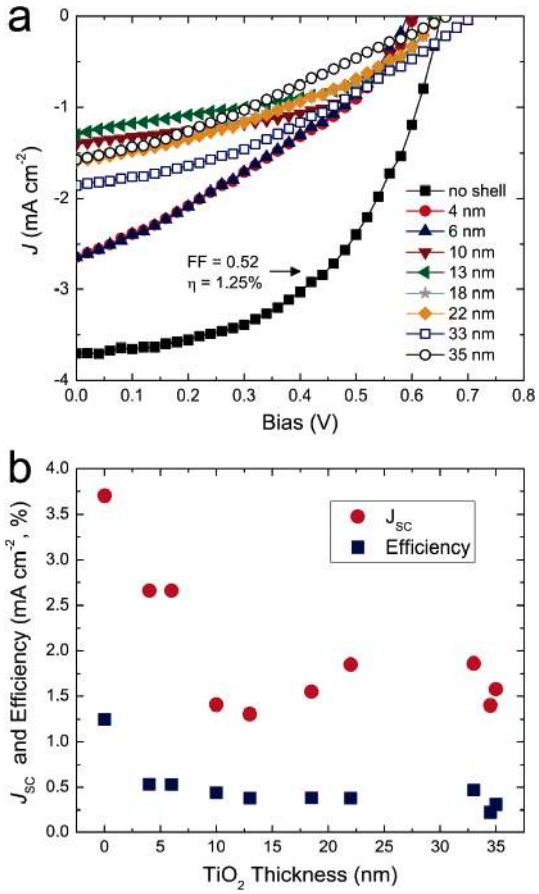

Figure 10. The performance of core−shell nanowire cells with amorphous TiO_2 shells. (a) Power plots. Shell thickness was determined by TEM. (b) J_{SC} and efficiency as a function of shell thickness. The other performance parameters can be found in the Supporting Information, Figure 2. Note that the trend in dye loading for these cells is similar to the trend found for the cells with crystalline shells, except that the dye loading does not slowly decrease at intermediate shell thicknesses.

of electron traps in amorphous titania slows electron transport and shortens the electron diffusion length. Thicker amorphous shells have a larger absolute number of traps but also a greater fraction of their volume farther from recombination sites on the nanowire surfaces. These opposing factors lead to a leveling off of J_{SC} for thick shells, as seen in Figure 10b. This comparison of anatase and amorphous shells strongly suggests that the J_{SC} recovery seen in Figure 7c is driven by shell crystallization.

At this point we can explain how the TiO_2 shells function and account for both the rapid increase in V_{OC} and fill factor and the sudden decrease and subsequent recovery of J_{SC} with increasing shell thickness. If one ignores the case of the 0.5-nm-thick shells, which may be discontinuous, it is clear from the trends in dark currents and shunt resistance that V_{OC} and fill factor increase because the TiO_2 shells suppress interfacial recombination. V_{OC} improves despite the poor electron injection yield of the amorphous and partially amorphous shells because the recombination rate falls by a larger factor than does the injection yield. In the absence of time-resolved measurements, we suppose that the shells suppress recombination by passivating surface recombination sites and by forming an energy barrier that prevents photoinjected electrons from approaching the nanowire surface. Since the band gaps and band edge energies of bulk ZnO and anatase TiO_2 are equal to within about 50 mV,[49,50] TiO_2 and ZnO can form an $n-n^+$ heterojunction free

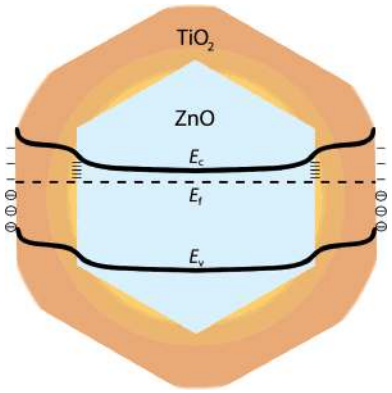

Figure 11. Schematic energy level diagram of a ZnO−TiO_2 core−shell nanowire in cross section and in equilibrium with the surrounding electrolyte.

of band discontinuities and with a built-in potential, neglecting any difference in densities of states, of

$$\phi_{bi} \approx V_{th} \ln \frac{N_D^+}{N_D}$$

where N_D^+ and N_D are the donor concentrations in the heavily doped ZnO core and more lightly doped TiO_2 shell, respectively.[51] An energy barrier of 75−150 mV is reasonable based on the likely doping difference between the ZnO and TiO_2. This radial field would reduce the electron concentration at the nanowire surface by a factor of $\exp(-\phi_{bi}/kT)$, or roughly 20−300 times smaller than the concentration at the center of a nanowire, which in turn would decrease the rate of recombination. A schematic band diagram of the proposed situation is given in Figure 11.

The complex trend in J_{SC} is best explained by considering three regimes of shell thickness. First, shells thinner than 5 nm are amorphous and probably electronically confined (while the exciton Bohr radius of amorphous titania is apparently unknown, that for anatase is probably 0.5−2 nm).[52−54] The thinnest shells also have a very high dye loading, which implies the presence of dye aggregates on the nanowires. These effects combine to cause poor electron injection, slow diffusion, and low J_{SC} values. The second regime covers shells 5−20-nm thick. Here, J_{SC} steadily improves because gradual crystallization of the shells results in better electron injection and fewer bulk and surface trap sites. Our data cannot distinguish between improved injection and transport, but it is sensible to expect that some combination of the two is responsible for the recovery in J_{SC}. Finally, cells with very thick shells show a slight falloff in J_{SC} because of a reduced surface area and smaller dye loading.

We attempted to fabricate core−shell cells of higher efficiency by using nanowire arrays of larger surface area. ZnO nanowire films were grown for up to twice the normal growth time and then coated in 20-nm-thick TiO_2 shells. However, this procedure failed to produce arrays of substantially higher surface area because the thicker nanowires coalesced to a greater degree upon addition of the TiO_2 shells. Our best DSCs made to date show only a 10−15% improvement in J_{SC} compared with the devices in Figure 6, with efficiencies of around 2.2% (Figure 12). One could minimize nanowire coalescence and attain larger film surface areas if much thinner, fully anatase shells could be grown. This is feasible by depositing the shells at higher temperatures (closer to 400 °C), but unwise considering the limitations of our current ALD system.

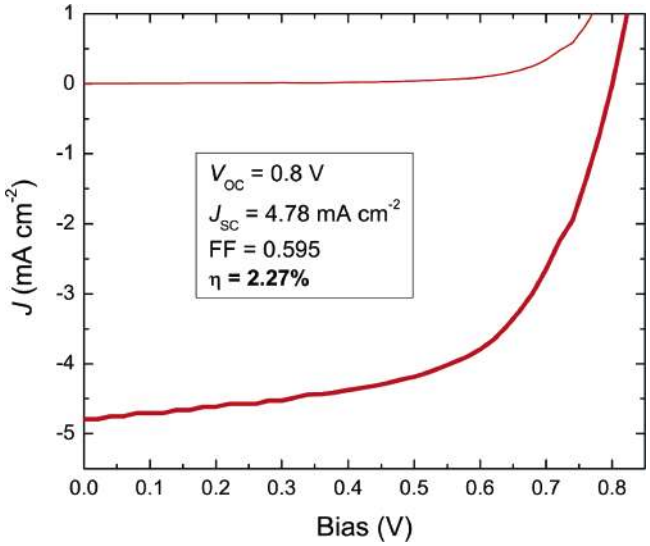

Figure 12. Dark and illuminated performance of a core−shell cell with an efficiency of 2.27%. Illuminated area: 0.3 cm^2.

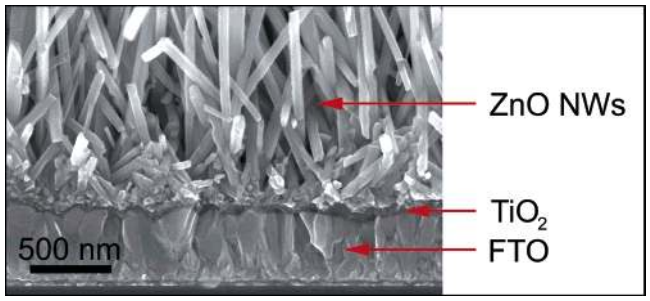

Figure 13. Cross-sectional SEM image of a ZnO nanowire array on TiO_2-coated FTO.

The Effect of Substrate-Based TiO_2 Layers on Nanowire and Nanoparticle Cells. Carrier recombination in DSCs can occur across both the film−electrolyte interface and the substrate−electrolyte interface. So far we have discussed modifying the film−electrolyte interface by way of oxide shells that are deposited conformally onto the nanowire arrays. In this section, we target recombination at the substrate−electrolyte interface by depositing TiO_2 blocking layers underneath the nanowire films. Thin, dense layers of anatase TiO_2 deposited on conducting glass by spray pyrolysis are routinely used in solid-state nanoparticle DSCs to prevent short circuiting between FTO and the hole transport medium.[56−58] Dedicated blocking layers are not as necessary in standard liquid electrolyte cells because of the large overvoltage for the reduction of I_3^- on FTO. Furthermore, high-efficiency electrolyte cells typically employ a $TiCl_4$ surface treatment that coats both the nanocrystalline film and any exposed FTO with ultrathin TiO_2, which itself acts to buffer FTO from the redox species. The investigation of compact TiO_2 layers in electrolyte cells began only recently and involves an ongoing debate.[59−62] Here we compare ALD-made TiO_2 blocking layers in nanowire and nanoparticle cells to highlight the differences between the two DSC architectures and to add to this debate.

ZnO nanowire cells and two types of TiO_2 nanoparticle cells were prepared on bare and TiO_2-coated FTO substrates. A cross-sectional image of a nanowire array on TiO_2-coated FTO is shown in Figure 13. The nanoparticle electrodes were made by spreading a commercial paste of 10−15 nm anatase crystals (Ti−Nanoxide T, Solaronix) on the substrates with a glass rod and sintering the films in air at 450 °C for 30 min (film thickness: 8−9 μm). One group of nanoparticle electrodes was then treated with $TiCl_4$, which is the standard treatment used to improve the J_{SC} of TiO_2 nanoparticle cells. The $TiCl_4$ treatment was performed by soaking each film in 50 mM aqueous $TiCl_4$ solution for 10 h in an airtight container at room temperature and then rinsing with water. All films were baked in air for 30 min (at 400 °C for the nanowire films and 450 °C for the nanoparticle films) immediately before dye sensitization.

Figure 14 shows the dark and photocurrent performance of the three types of DSCs for TiO_2 underlayer thicknesses of 0, 10, 25, and 50 nm. Each curve is the average of three nominally identical devices. The nanoparticle cells not treated with $TiCl_4$ show slight improvements in J_{SC}, V_{OC}, and fill factor with increasing layer thickness, resulting in a 25% enhancement in conversion efficiency (to 3.3%; Figure 14a), in rough agreement with previous results.[62] The addition of an underlayer suppresses the dark current of these cells at biases negative of V_{OC} (Figure 14b). The 100-fold decrease in the anodic exchange current (the current at negative bias) suggests that electron transfer from the electrolyte to FTO is blocked by the TiO_2 layer. Likewise, the lower dark cathodic recombination current (the current at positive bias) indicates that electron transfer from FTO to I_3^- is slowed by the layer (Figure 14c). Reduced rates of recombination cause the improved performance of these untreated TiO_2 cells.

In contrast, the $TiCl_4$-treated nanoparticle cells show a loss of J_{SC} with increasing blocking layer thickness, while V_{OC} and fill factor are unaffected, resulting in a 10% loss in efficiency (to 3.2%; Figure 14d). The underlayers again cause a drastic decrease in exchange current, but only a relatively small reduction in recombination current at biases negative of 0.4 V (Figure 14e,f). We attribute the smaller effect of these layers to the lower initial recombination rate of the $TiCl_4$-treated devices. The $TiCl_4$ treatment probably passivates the most active recombination sites on the exposed FTO surface, rendering additional TiO_2 layers ineffectual, even counterproductive. Under illumination, these blocking layers add to the series resistance and reduce the J_{SC} of these cells.

Our data provide some insight into the role of the $TiCl_4$ surface treatment. We find that it improves J_{SC} by ~50% but lowers the fill factor compared to identical, untreated devices (see Figure 14a,d and the Supporting Information, Figure 4). Absorption spectra of stained films and solutions of dye desorbed from these films show that the $TiCl_4$ treatment causes a slight reduction in dye loading (Supporting Information, Figure 4). Therefore, the larger J_{SC} must stem from some combination of more efficient electron injection into the nanocrystalline film and more efficient electron collection by FTO. Better injection can result if the pure TiO_2 layer deposited from $TiCl_4$ disfavors the formation of weakly bound dye molecules and dye aggregates. At the same time, better electron collection is possible if the $TiCl_4$-derived TiO_2 layer reduces the probability of photoinjected electrons recombining with triiodide. This may occur by a combination of improved interparticle connectivity (neck thickening) and a lower density of recombination sites on the purer TiO_2 surface. We note that our findings are at odds with a recent report that attributes the larger J_{SC} to an enhanced dye loading;[61] this disagreement almost certainly reflects differences in the surface properties of the nanoparticle films used in these two studies.

We now turn to the effect of the TiO_2 blocking layers on the ZnO nanowire cells. Here J_{SC} falls by 25% upon addition of an underlayer, while V_{OC} improves slightly with layer thickness

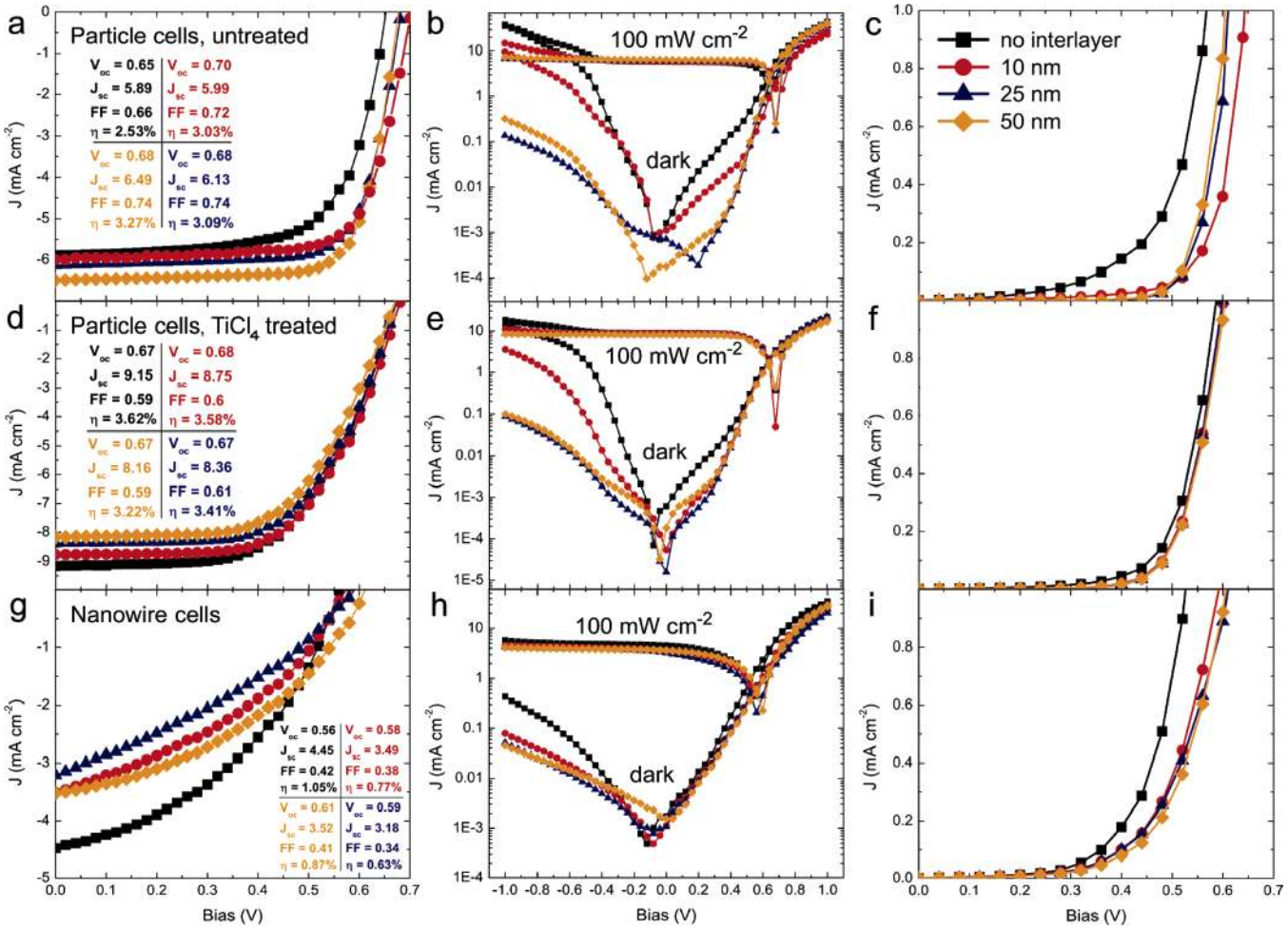

Figure 14. Current−voltage plots for (a−c) TiO_2 nanoparticle cells without the $TiCl_4$ surface treatment, (d−f) TiO_2 nanoparticle cells with the $TiCl_4$ treatment, and (g−i) ZnO nanowire cells, for TiO_2 underlayer thicknesses of 0, 10, 25, and 50 nm. Curves are averages of three identically prepared devices. The legend in part c applies to every plot. The first column shows power plots. Insets tabulate the averaged efficiency characteristics of the devices (clockwise from upper left: underlayer thicknesses from 0 to 50 nm). The second column shows complete dark and illuminated curves on a semilogarithmic scale. The third column shows dark recombination current on a linear scale. Additional characterization of the TiO_2 layers can be found in the Supporting Information, Figure 3.

and the fill factor first declines and then recovers, resulting overall in a 20% loss of efficiency (to 0.87%; Figure 14g). The dark exchange current drops 10-fold and the recombination current is suppressed by a factor of 2−3 at biases negative of V_{OC} (Figure 14h,i). Relative to the nanoparticle cells, the dark current of the nanowire cells is much less responsive to the addition of TiO_2 layers because these cells feature a dense layer of ZnO that forms at the base of the nanowire film during growth.[21] The electrolyte therefore contacts not FTO but ZnO, which partially blocks the dark current. J_{SC} falls despite a smaller recombination current probably as a result of the same energy barrier at the ZnO−TiO_2 interface that suppresses recombination in the core−shell nanowire cells.

We draw several conclusions from the experiments in this section. First, substrate-based blocking layers primarily benefit inefficient nanoparticle cells, especially those not treated with $TiCl_4$. Second, nanoparticle DSC performance is anomalously insensitive to the magnitude of the dark exchange current. Third, the $TiCl_4$ treatment improves electron injection or transport rather than light absorption, at least for the moderately efficient nanocrystalline films used here. Finally, modifying the FTO surface is not a promising approach to improving the performance of nanowire DSCs in which a dense blocking layer already exists.

Conclusions

ZnO−Al_2O_3 and ZnO−TiO_2 core−shell nanowire dye-sensitized solar cells have been fabricated and compared to cells built from ZnO nanowires without shells. Thin Al_2O_3 shells act as tunnel barriers that reduce recombination only at the expense of a larger reduction in electron injection yield and a lower device efficiency. TiO_2 shells suppress recombination and markedly improve cell open-circuit voltage and fill factor. On the basis of trends in the relevant performance parameters as a function of TiO_2 thickness, we attribute these effects to the passivation of surface recombination sites and the buildup of a radial energy barrier that repels electrons from the nanowire surface. Meanwhile, the valley-to-peak trend in short-circuit current is consistent with the notion that the higher crystallinity of thicker shells enables more efficient electron injection and transport. Tests of cells with thick amorphous shells confirm that large currents are obtained only with crystalline TiO_2 shells. ZnO−TiO_2 core−shell cells of optimal shell thickness and nanowire surface area achieve an efficiency of 2.25% under full sunlight. Higher efficiencies require nanowire films of larger surface area. This is best achieved by synthesizing denser arrays of thinner nanowires, rather than increasing nanowire length or diameter. For example, a hexagonal lattice of core−shell nanowires with lengths of 30 μm, a core diameter of 40 nm, a

shell thickness of 5 nm, and a pitch of 70 nm would have a surface area equal to that of a typical nanocrystalline film.

Depositing a layer of anatase TiO_2 under rather than on the nanowire films reduces dark currents only slightly because these cells already feature a thin blocking layer of ZnO at their base. Adding TiO_2 underlayers to these cells decreases both their photocurrent and efficiency, probably as a consequence of the same energy barrier at the ZnO−TiO_2 interface that suppresses recombination in the core−shell nanowire cells. The response of TiO_2 nanoparticle cells to the blocking layers depends on whether the nanoparticle films are treated with $TiCl_4$ before dye sensitization.

There are three reasons to believe that nanowire films may be superior to nanoparticle films in DSCs. First, nanowire films are more easily filled with the nonvolatile hole conductors needed for improved device stability. Second, electron transport within single-crystalline nanowires can be much faster than transport through nanocrystalline networks. Third, surface fields within each nanowire can be used to enforce charge separation and thereby ensure that faster transport results in a longer diffusion length. Nanoparticle DSCs lack such surface fields. Here we have presented strong but indirect evidence for the existence and importance of a surface field in core−shell nanowire DSCs, and our findings should be followed up by direct measurements of electron diffusivity and lifetime with use of time-resolved methods such as intensity modulated photocurrent and photovoltage spectroscopy. Further work is also needed to ascertain the degree to which electron injection yields depend on oxide crystallinity. Application of the core−shell concept to nanowire photoelectrodes is in an early stage and much room for optimization exists.

Acknowledgment. This work was supported by the Department of Energy, Office of Basic Sciences, the University of California, Berkeley, the Hellman Family Fund, the Sloan Foundation, the Searle Foundation, and the Department of Energy, Energy Biosciences Program. M.L. and L.E.G. are Berkeley-ITRI Fellows. We thank the National Center for Electron Microscopy for the use of their facilities.

Supporting Information Available: XRD and TEM data of amorphous TiO_2 nanotubes and the amorphous−anatase phase transition, performance trends for cells with amorphous TiO_2 shells, characterization of TiO_2 thin films on FTO substrates, and $J-V$ measurements showing the effect of the $TiCl_4$ treatment. This material is available free of charge via the Internet at http://pubs.acs.org.

References and Notes

(1) Kopidakis, N.; Benkstein, K. D.; van de Lagemaat, J.; Frank, A. J. *J. Phys. Chem. B* **2003**, *107*, 11307.

(2) Nazeeruddin, M. K.; Kay, A.; Rodicio, I.; Humphry-Baker, R.; Müller, E.; Liska, P.; Vlachopoulos, N.; Grätzel, M. *J. Am. Chem. Soc.* **1993**, *115*, 6382.

(3) Gregg, B. A.; Pichot, F.; Ferrere, S.; Fields, C. L. *J. Phys. Chem. B* **2001**, *105*, 1422.

(4) Grätzel, M. *Inorg. Chem*. **2005**, *44*, 6841.

(5) Kubo, W.; Kitamura, T.; Hanabusa, K.; Wada, Y.; Yanagida, S. *Chem. Commun*. **2002**, 374.

(6) Mazille, F.; Fei, Z.; Kuang, D.; Zhao, D.; Zakeeruddin, S. M.; Grätzel, M.; Dyson, P. J. *Inorg. Chem*. **2006**, *45*, 1585.

(7) Krûger, J.; Plass, R.; Grätzel, M.; Cameron, P. J.; Peter, L. M. *J. Phys. Chem. B* **2003**, *107*, 7536.

(8) Wang, P.; Zakeeruddin, S. M.; Moser, J. E.; Nazeeruddin, M. K.; Sekiguchi, T.; Grätzel, M. *Nature Mater*. **2003**, *2*, 402.

(9) Schmidt-Mende, L.; Bach, U.; Humphry-Baker, R.; Horiuchi, T.; Miura, H.; Ito, S.; Uchida, S.; Grätzel, M. *Adv. Mater.* **2005**, *17*, 813.

(10) Kuang, D.; Ito, S.; Wenger, B.; Klein, C.; Moser, J.-E.; Humphry-Baker, R.; Zakeeruddin, S. M.; Grätzel, M. *J. Am. Chem. Soc*. **2006**, *128*, 4146.

(11) Hara, K.; Wang, Z.-S.; Sato, T.; Furube, A.; Katoh, R.; Sugihara, H.; Dan-oh, Y.; Kasada, C.; Shinpo, A.; Suga, S. *J. Phys. Chem. B* **2005**, *109*, 15476.

(12) Horiuchi, T.; Miura, H.; Sumioka, K.; Uchida, S. *J. Am. Chem. Soc.* **2004**, *126*, 12218.

(13) Altobello, S.; Argazzi, R.; Caramori, S.; Contado, C.; Da Fré, S.; Rubino, P.; Choné, C.; Larramona, G.; Bignozzi, C. A. *J. Am. Chem. Soc.* **2005**, *127*, 15342.

(14) Robertson, N. *Angew. Chem., Int. Ed*. **2006**, *45*, 2338.

(15) Dloczik, L.; Ileperuma, O.; Lauermann, I.; Peter, L. M.; Ponomarev, E. A.; Redmond, G.; Shaw, N. J.; Uhlendorf, I. *J. Phys. Chem. B* **1997**, *101*, 10281.

(16) Fisher, A. C.; Peter, L. M.; Ponomarev, E. A.; Walker, A. B.; Wijayantha, K. G. U. *J. Phys. Chem. B* **2000**, *104*, 949.

(17) Nakade, S.; Matsuda, M.; Kambe, S.; Saito, Y.; Kitamura, T.; Sakata, T.; Wada, Y.; Mori, H.; Yanagida, S. *J. Phys. Chem. B* **2004**, *106*, 10004.

(18) Grätzel, M. *J. Photochem. Photobiol. A*: *Chem*. **2004**, *164*, 3.

(19) Zukalová, M.; Zukal, A.; Kavan, L.; Nazeeruddin, M. K.; Liska, P.; Grätzel, M. *Nano Lett*. **2005**, *5*, 1789.

(20) Green, A. N. M.; Palomares, E.; Haque, S. A.; Kroon, J. M.; Durrant, J. R. *J. Phys. Chem. B* **2005**, *109*, 12525.

(21) Law, M.; Greene, L. E.; Johnson, J. C.; Saykally, R.; Yang, P. *Nat. Mater.* **2005**, *4*, 455.

(22) Adachi, M.; Murata, Y.; Takao, J.; Jiu, J.; Sakamoto, M.; Wang, F. *J. Am. Chem. Soc.* **2004**, *126*, 14943.

(23) Jiu, J.; Isoda, S.; Wang, F.; Adachi, M. *J. Phys. Chem. B* **2006**, *110*, 2087.

(24) Ohsaki, Y.; Masaki, N.; Kitamura, T.; Wada, Y.; Okamoto, T.; Sekino, T.; Niihara, K.; Yanagida, S. *Phys. Chem. Chem. Phys.* **2005**, *7*, 4157.

(25) Mor, G. K.; Shankar, K.; Paulose, M.; Varghese, O. K.; Grimes, C. A. *Nano Lett*. **2006**, *6*, 215.

(26) Baxter, J. B.; Aydil, E. S. *Appl. Phys. Lett.* **2005**, *86*, 053114.

(27) Zaban, A.; Chen, S. G.; Chappel, S.; Gregg, B. A. *Chem. Commun*. **2000**, 2231.

(28) Tennakone, K.; Bandara, J.; Bandaranayake, P. K. M.; Kumara, G. R. A.; Konno, A. *Jpn. J. Appl. Phys*. **2001**, *40*, L732.

(29) Palomares, E.; Clifford, J. N.; Haque, S. A.; Lutz, T.; Durrant, J. R. *J. Am. Chem. Soc.* **2003**, *125*, 475.

(30) Diamant, Y.; Chappel, S.; Chen S. G.; Melamed, O.; Zaban, A. *Coord. Chem. Rev.* **2004**, *248*, 1271.

(31) Diamant, Y.; Chen, S. G.; Melamed, O.; Zaban, A. *J. Phys. Chem. B* **2003**, *107*, 1977.

(32) Bandaranayake, K. M. P.; Senevirathna, M. K. I.; Weligamuwa, P. M. G. M. P.; Tennakone, K. *Coord. Chem. Rev.* **2004**, *248*, 1277.

(33) Min, B.; Lee, J. S.; Cho, K.; Hwang, J. W.; Kim, H.; Sung, M. Y.; Kim, S.; Park, J.; Seo, H. W.; Bae, S. Y.; Lee, M.-S.; Park, S. O.; Moon, J.-T. *J. Electron. Mater.* **2003**, *32*, 1344.

(34) Hwang, J.; Min, B.; Lee, J. S.; Keem, K.; Cho, K.; Sung, M.-Y.; Lee, M.-S.; Kim, S. *Adv. Mater.* **2004**, *16*, 422.

(35) Kumara, G. R. R. A.; Tennakone, K.; Perera, V. P. S.; Konno, A.; Kaneko, S.; Okuya, M. *J. Phys. D*: *Appl. Phys*. **2001**, *34*, 868.

(36) Zhang, X.; Sutanto, I.; Taguchi, T.; Tokuhiro, K.; Meng, Q.; Rao, T. N.; Fujishima, A.; Watanabe, H.; Nakamori, T.; Uragami, M. *Solar. Energy Mater. Solar Cells* **2003**, *80*, 315.

(37) O'Regan, B. C.; Scully, S.; Mayer, A. C.; Palomares, E.; Durrant, J. *J. Phys. Chem. B* **2005**, *109*, 4616

(38) Lenzmann, F.; Nanu, M.; Kijatkina, O.; Belaidi, A. *Thin Solid Films* **2004**, *451*−*452*, 639.

(39) Fabregat-Santiago, F.; Garcia-Canadas, J.; Palomares, E.; Clifford, J. N.; Haque, S. A.; Durrant, J. R.; Garcia-Belmonte, G.; Bisquert, J. *J. Appl. Phys.* **2004**, *96*, 6903.

(40) Ritala, M.; Leskelä, M.; Nykänen, E.; Soininen, P.; Niinistö, L. *Thin Solid Films* **1993**, *225*, 288.

(41) Mitchell, D. R. G.; Triani, G.; Attard, D. J.; Finnie, K. S.; Evans, P. J.; Barbé, C. J.; Bartlett, J. R. *Proc. SPIE* **2004**, *5276*, 296.

(42) Aarik, J.; Aidla, A.; Uustare, T.; Sammelselg, V. *J. Cryst. Growth* **1995**, *148*, 268.

(43) Mitchell, D. R. G.; Attard, D. J.; Triani, G. *Thin Solid Films* **2003**, *441*, 85.

(44) Horiuchi, H.; Katoh, R.; Hara, K.; Yanagida, M.; Murata, S.; Arakawa, H.; Tachiya, M. *J. Phys. Chem. B* **2003**, *107*, 2570.

(45) From dye desorption measurements of core−shell nanowire films with 20-nm-thick anatase or amorphous shells sensitized for 12 h, we estimate the dye loading on amorphous titania to be about twice that of anatase titania.

(46) Martini, I.; Hodak, J. H.; Hartland, G. V. *J. Phys. Chem. B* **1998**, *102*, 9508.

(47) Benkö, G.; Skårman, B.; Wallenberg, R.; Hagfeldt, A.; Sundström, V.; Yartsev, A. P. *J. Phys. Chem. B* **2003**, *107*, 1370.
(48) Kallionen, J.; Benkö, G.; Myllyperkiö, P.; Khriachtchev, L.; Skårman, B.; Wallenberg, R.; Tuomikoski, M.; Korppi-Tommola, J.; Sundström, V.; Yartsev, A. P. *J. Phys. Chem. B* **2004**, *108*, 6365.
(49) Xu, Y.; Schoonen, M. A. A. *Am. Mineral.* **2000**, *85*, 543.
(50) Grätzel, M. *Nature* (*London*) **2001**, *414*, 338.
(51) von Roos, O. *J. Appl. Phys.* **1978**, *49*, 3503.
(52) Kormann, C.; Bahnemann, D. W.; Hoffmann, M. R. *J. Phys. Chem.* **1988**, *92*, 5196.
(53) Tang, H.; Prasad, K.; Sanjinès, R.; Schmid, P. E.; Lévy, F. *J. Appl. Phys.* **1994**, *75*, 2042.
(54) Serpone, N.; Lawless, D.; Khairutdinov, R. *J. Phys. Chem. B* **1995**, *99*, 16646.
(55) Monticone, S.; Tufeu, R.; Kanaev, A. V.; Scolan, E.; Sanchez, C. *Appl. Phys. Sci.* **2000**, *162*−*163*, 565.
(56) Kavan, L.; Grätzel, M. *Electrochim. Acta* **1995**, *40*, 643.
(57) Bach, U.; Lupo, D.; Comte, P.; Moser, J. E.; Weissörtel, F.; Salbeck, J.; Spreitzer, H.; Grätzel, M. *Nature* (*London*) **1998**, *395*, 583.
(58) Peng, B.; Jungmann, G.; Jäger, C.; Haarer, D.; Schmidt, H.-W.; Thelakkat, M. *Coord. Chem. Rev.* **2004**, *248*, 1479.
(59) Cameron, P. J.; Peter, L. M. *J. Phys. Chem. B* **2003**, *107*, 14394.
(60) Cameron, P. J.; Peter, L. M.; Hore, S. *J. Phys. Chem. B* **2005**, *109*, 930.
(61) Ito, S.; Liska, P.; Comte, P.; Charvet, R.; Péchy, P.; Bach, U.; Schmidt-Mende, L.; Zakeeruddin, S. M.; Kay, A.; Nazeeruddin, M. K.; Grätzel, M. *Chem. Commun*. **2005**, 4351.
(62) Hore, S.; Kern, R. *Appl. Phys. Lett.* **2005**, *87*, 263504.